Research Article | Vol. 25, No. 8 | 17 Apr 2017 | OPTICS EXPRESS 8896

Optics EXPRESS

Passively-coupled, low-coherence interferometric duct profiling with an astigmatism-corrected conical mirror

HELEN D. FORD* AND RALPH P. TATAM

Centre for Engineering Photonics, Cranfield University, College Road, Cranfield, MK43 0AL, UK
*h.d.ford@cranfield.ac.uk

Abstract: Duct-profiling in test samples up to 25 mm in diameter has been demonstrated using a passive, low-coherence probe head with a depth resolution of 7.8 μm, incorporating an optical-fibre-linked conical mirror addressed by a custom-built array of single-mode fibres. Zemax modelling, and experimental assessment of instrument performance, show that degradation of focus, resulting from astigmatism introduced by the conical mirror, is mitigated by the introduction of a novel lens element. This enables a good beam focus to be achieved at distances of tens of millimetres from the cone axis, not achievable when the cone is used alone. Incorporation of the additional lens element is shown to provide a four-fold improvement in lateral imaging resolution, when compared with reflection from the conical mirror alone.

Published by The Optical Society under the terms of the Creative Commons Attribution 4.0 License. Further distribution of this work must maintain attribution to the author(s) and the published article's title, journal citation, and DOI.

OCIS codes: (060.2350) Fiber optics imaging; (060.2370) Fiber optics sensors; (080.4228) Nonspherical mirror surfaces; (110.4500) Optical coherence tomography; (120.3930) Metrological instrumentation.

References and links

1. B. L. Danielson and C. Y. Boisrobert, "Absolute optical ranging using low coherence interferometry," Appl. Opt. **30**(21), 2975–2979 (1991).
2. Y.-J. Rao and D. A. Jackson, "Recent progress in fibre optic low-coherence interferometry," Meas. Sci. Technol. **7**(7), 981–999 (1996).
3. I. Balboa, H. D. Ford, and R. P. Tatam, "Low-coherence optical fibre speckle interferometry," Meas. Sci. Technol. **17**(4), 605–616 (2006).
4. J. A. Izatt and M. A. Choma, "Theory of Optical Coherence Tomography" in *Optical Coherence Tomography*, W. Drexler and J. G. Fujimoto eds. (Springer, 2008).
5. D. Huang, E. A. Swanson, C. P. Lin, J. S. Schuman, W. G. Stinson, W. Chang, M. R. Hee, T. Flotte, K. Gregory, C. A. Puliafito, and J. G. Fujimoto, "Optical coherence tomography," Science **254**(5035), 1178–1181 (1991).
6. A. M. Zysk, F. T. Nguyen, A. L. Oldenburg, D. L. Marks, and S. A. Boppart, "Optical coherence tomography: a review of clinical development from bench to bedside," J. Biomed. Opt. **12**(5), 051403 (2007).
7. M. V. Sivak, Jr., K. Kobayashi, J. A. Izatt, A. M. Rollins, R. Ung-Runyawee, A. Chak, R. C. Wong, G. A. Isenberg, and J. Willis, "High-resolution endoscopic imaging of the GI tract using optical coherence tomography," Gastrointest. Endosc. **51**(4), 474–479 (2000).
8. J. Armstrong, M. Leigh, I. Walton, A. Zvyagin, S. Alexandrov, S. Schwer, D. Sampson, D. Hillman, and P. Eastwood, "In vivo size and shape measurement of large hollow organs using endoscopic long-range optical coherence tomography," Opt. Express **11**(15), 1817–1826 (2003).
9. B. C. Quirk, R. A. McLaughlin, A. Curatolo, R. W. Kirk, P. B. Noble, and D. D. Sampson, "In situ imaging of lung alveoli with an optical coherence tomography needle probe," J. Biomed. Opt. **16**(3), 036009 (2011).
10. P. H. Tran, D. S. Mukai, M. Brenner, and Z. Chen, "In vivo endoscopic optical coherence tomography by use of a rotational microelectromechanical system probe," Opt. Lett. **29**(11), 1236–1238 (2004).
11. D. Southwell, B. Vandegriend, and A. Basu, "A conical mirror pipeline inspection system" in *Proceedings of IEEE International Conference on Robotics and Automation* (IEEE 1996), pp, 3253–3258.
12. A. A. Gonçalves, Jr. and M. R. Viotti, "Radial Speckle Interferometry and Applications," in *Advances in Speckle Metrology and Related Techniques*, G. H. Kaufmann ed. (Wiley, 2011)
13. R. Isago and K. Nakamura, "High-speed imaging with endoscopic optical coherence tomography using bending vibration of optical fiber," Proc. SPIE **7503**, 75034Y (2009).
14. H. D. Ford and R. P. Tatam, "Characterization of optical fiber imaging bundles for swept-source optical coherence tomography," Appl. Opt. **50**(5), 627–640 (2011).

#285603 https://doi.org/10.1364/OE.25.008896
Journal © 2017 Received 26 Jan 2017; revised 22 Mar 2017; accepted 25 Mar 2017; published 6 Apr 2017

Optics EXPRESS

15. H. D. Ford and R. P. Tatam, "Full-field optical coherence tomography using a fibre imaging bundle," Proc. SPIE **6079**, 60791H (2006).
16. T. Xie, D. Mukai, S. Guo, M. Brenner, and Z. Chen, "Fiber-optic-bundle-based optical coherence tomography," Opt. Lett. **30**(14), 1803–1805 (2005).
17. H. D. Ford and R. P. Tatam, "Fibre imaging bundles for full-field optical coherence tomography," Meas. Sci. Technol. **18**(9), 2949–2957 (2007).
18. H. D. Ford and R. P. Tatam, "Passive OCT probe head for 3D duct inspection," Meas. Sci. Technol. **24**(9), 094001 (2013).
19. J. J. Armstrong, M. S. Leigh, J. H. Walsh, D. R. Hillman, P. R. Eastwood, and D. D. Sampson, "Anatomical optical coherence tomography for imaging the human upper airway," in *Optical Coherence Tomography Technology and Applications*, W. Drexler, J. G. Fujimoto eds. (Springer, 2008).
20. Recommended practice RPO501, erosive wear in piping systems. Revision 4.2 2007, Det Norske Veritas, *https://rules.dnvgl.com/docs/pdf/DNV/codes/docs/2011-01/RP-O501.pdf*.
21. D. R. Adams, "Tribological considerations in internal combustion engines," in *Tribology and Dynamics of Engine and Powertrain: Fundamentals, Applications and Future Trends*, H. Rahnejat ed. (Woodhead, 2010).
22. M. de Rosa, J. Carberry, V. Bhagavatula, K. Wagner, and C. Saravanos, "High-power performance of single-mode fibre-optic connectors," J. Lightwave Technol. **20**(5), 879–885 (2002).
23. I. Durazo-Cardenas, P. Shore, X. Luo, T. Jacklin, S. A. Impey, and A. Cox, "3D characterisation of tool wear whilst diamond turning silicon," Wear **262**(3–4), 340–349 (2006).
24. E. Hecht and A. Zajac, "More on geometrical optics," in *Optics*, (Addison-Wesley, 1974), Ch. 6.
25. R. Leitgeb, W. Drexler, A. Unterhuber, B. Hermann, T. Bajraszewski, T. Le, A. Stingl, and A. Fercher, "Ultrahigh resolution Fourier domain optical coherence tomography," Opt. Express **12**(10), 2156–2165 (2004).
26. L. P. Hariri, B. E. Bouma, S. Waxman, M. Shishkov, B. J. Vakoc, M. J. Suter, M. I. Freilich, W.-Y. Oh, M. Rosenberg, and G. J. Tearney, "An automatic image processing algorithm for initiating and terminating intracoronary OFDI pullback," Biomed. Opt. Express **1**(2), 566–573 (2010).

1. Introduction

Low-coherence interferometry (LCI) is an optical technique for surface profiling [1–3], capable of spatial resolution down to a few μm and depth resolution down to around 1 μm, or considerably better for single surfaces smooth on the scale of the optical wavelength [4]. When the target is a semi-transparent, often biological, material and light penetrates below the surface to form an image of sub-surface structures, the adapted method is called optical coherence tomography (OCT) [5,6]. Both LCI and OCT can be configured either as benchtop systems, which offer the highest spatial resolutions, or as endoscopic, fibre-delivered systems for internal investigations of hollow spaces [7,8].

In endoscopic OCT, an optical-fibre-linked endoscope probe is typically introduced into a quasi-cylindrical vessel of the body such as the oesophagus, the trachea or an artery. Such a probe can be configured either for forward imaging or for sideways imaging. In sideways mode, the forward-pointing probe beam is typically reflected through an angle of 90° to image tissue lying alongside the probe, using a fixed or electrically-controlled 45° turning mirror in combination with a rotation of the mirror or of the entire probe. This allows the beam to acquire a data set around a circumference of the vessel of interest [9,10].

Conical mirrors have previously been proposed and investigated for pipeline inspection [11,12], but the first proposal for use of a conical instead of a planar reflector in OCT was made in 2009, demonstrated using an optical fibre mounted on a piezoelectric actuator to sweep the fibre tip in a circle and address different positions on the cone surface [13]. Alternative configurations with optical-fibre bundles, resulting in passive probe heads, have been demonstrated by ourselves and others [14–17], one of which uses a fibre imaging bundle combined with a conical mirror to move the scanning from the probe tip to a remote region outside the endoscope, thus avoiding the requirement for miniaturised moving components at the tip of the instrument [18]. A schematic of this system is shown in Fig. 1.

Commercial bundles, however, are not generally designed to provide single-mode fibre performance. Multi-moding causes difficulties in the interferometric system, so the current work uses instead a custom array manufactured in-house from single-mode optical fibre.

Optics EXPRESS

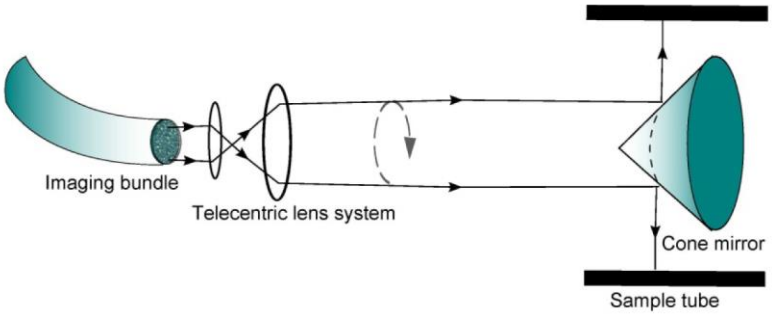

Fig. 1. Conical mirror in typical geometry used for low-coherence duct inspection, showing two incident beams, each turned through 90° to address duct wall.

Existing conical-mirror OCT instruments will be limited by defocus of the tangential component of the incident beam, caused by the high surface curvature of the very small conical mirror used to ensure a small probe diameter for endoscopic applications. A large degree of astigmatism is introduced into the beam reflected from the cone, preventing the formation of a tightly-focused spot in the imaging region. There is a significant reduction of lateral resolution, even at distances of only a few mm from the cone surface, compared with reflection from a plane surface. This paper describes a method to compensate the astigmatism, improving the lateral resolution and signal magnitude in conical-mirror imaging techniques.

There are two modes of use in which a conical mirror-based system could be advantageous for low-coherence measurements. The first is a technique sometimes known as anatomical OCT [19], in which OCT imaging is employed over a relatively long working distance to measure the internal surface profile of a quasi-cylindrical duct. The main application of this technique to date has been *in-vivo* dynamic mapping of the internal profiles of tubes of the respiratory system, for which a lateral resolution of around 100 μm appears to be adequate at a working distance of many millimetres. The numerical aperture (NA) of the probe beam, for the long working distance required, is low, implying a correspondingly low lateral resolution, but the limitation is not important in this application where a high-resolution image is not essential. Endoscopic medical probes are also of interest in the more usual high-resolution sub-surface OCT imaging mode. In this case, with probe diameters of just a few millimetres, the astigmatism introduced by the cone curvature would currently require that a conical mirror probe be positioned closely adjacent to the sample surface to obtain a high NA and sufficient spatial resolution for high-quality imaging.

Engineering applications exist, as well as medical, in which internal profiling measurements are of interest; in the oil, gas and water industries, internal pipe inspections during construction or maintenance can help to identify defects. For example, when oil is extracted from oil sands, abrasion of the sand on the internal surfaces of pipes, particularly at bends, can result in wall-thinning [20]. The high depth resolution of LCI would be ideal for detection of this and other internal defects at an early stage, during laboratory research, in small-diameter plant piping and possibly also in higher-diameter pipelines. In oil or gas pipe applications, explosive working environments occur for which a passive probe would be beneficial. Another possible application is high-resolution profiling in tubing for which circular symmetry is crucial, such as in mating pipework parts or pistons [21]. The lack of a rotating joint in the imaging probe will help here for high-resolution measurements, in avoiding potential centration errors that can arise during rotation.

Other possibilities for the use of astigmatism-corrected conical mirrors include endoscopic delivery of therapeutic optical beams for medical purposes, such as cauterisation of internal endothelial surfaces, or analogous engineering situations such as laser welding or ablation within cylindrical pipework. The avoidance of butt-coupled optical fibre joints is particularly

Optics EXPRESS

advantageous during delivery of higher-powered beams where optically-induced fibre damage can sometimes occur, especially when surfaces become contaminated [22].

Here, a conical mirror OCT system including a custom-made cylindrical lens to reduce beam astigmatism is proposed and demonstrated. Expected performance has been modelled using ray-tracing software, and modelling results are compared with the outcome of measurements made using a prototype benchtop probe. Working distances ranging from a few millimetres from the probe surface to a few tens of millimetres have been considered in modelling the behaviour of such systems, and we address their potential for both profiling and imaging applications. Our prototype system is a 'passive probe', in which the conical mirror is addressed by an array of single-mode fibres arranged on the circumference of a quarter-circle. This avoids the requirement for beam-scanning within the body of the probe, all scanning components being placed anterior to the input end of the fibre array. In this type of probe with a fixed number of sampling points, lateral resolution decreases as the working distance increases, but the sampling rate relative to the circumference of the duct remains constant. However, the astigmatism analysis below would apply equally to a scanned system in which a single input beam is moved to address different positions on the cone surface.

2. Mathematics of reflection at a conical surface

When a convergent beam is reflected from a plane mirror, the direction of the chief ray is altered but the beam convergence angle is unchanged following reflection. However, for the same beam reflected from a curved surface, the convergence angle after reflection, in any plane containing the chief ray, depends upon the radius of curvature in that plane at the point of reflection.

In this investigation we consider reflection from a conical (axicon) mirror. For optical sensing applications in quasi-cylindrical ducts, we are interested primarily in incident beams where the chief ray travels parallel to the axis of a 45° cone co-axial with the duct.

The incident beam is reflected through 90°, such that the chief ray follows a radial path towards the wall of the duct under inspection. Light scattered from the duct surface follows the reciprocal path, being collected by a detection system close to the duct axis. Analyses below are specific to this situation, and consider only incident rays parallel to the cone axis.

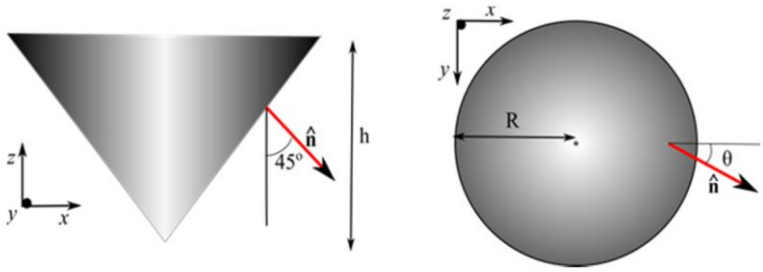

Fig. 2. Side-on (left) and end-on (right) views of a 45° conical mirror of base radius R and height h, showing a unit vector $\hat{\mathbf{n}}$ normal to the cone surface and the Cartesian co-ordinate system used in beam reflection calculations.

Reflection angles are efficiently calculated using vector algebra. We designate a Cartesian co-ordinate system, shown in Fig. 2, in which x and y lie parallel to the cone base, and z parallel to the cone axis, with the co-ordinate origin at the cone tip. For a cone of base radius R and height h, the radius at a distance z from the cone tip is $r = zR/h$. For the cone used in this investigation, both the height and the base diameter are 10 mm, therefore $R = h$ and the cone base angle is 45°. Thus the surface normal in any plane passing through the z-axis lies at 45° to the axis and $z = r$ at all distances from the cone tip.

Optics EXPRESS

The surface normal is always at 45° to the *z*-axis and forms an angle, which we call θ, with the *x*-axis, yielding direction cosines $x = \cos\theta/\sqrt{2}$ and $y = \sin\theta/\sqrt{2}$. The general unit vector $\hat{\mathbf{n}}$ defining the surface normal is therefore

$$\hat{n} = \frac{1}{\sqrt{2}}(\cos\theta, \sin\theta, -1). \tag{1}$$

For beams travelling parallel to the *z*-axis and intersecting the cone at a known radius, circular symmetry implies that we need study the process of reflection at only one position to understand the effect of the mirror curvature on all related beams incident at the same radius. To simplify calculations, we choose one of the two positions where $y = 0$ and specify that the centre of the incident beam intersects the cone at (r, 0, r). If the incident beam is convergent, with a half-angle φ, then the incident numerical aperture $NA_{incident} = \sin\varphi$. The unit direction vectors for incident marginal rays parallel to the cone axis are $\hat{\mathbf{i}}_a = (\mp\sin\varphi, 0, \cos\varphi)$, and for rays parallel to the local cone tangent are $\hat{\mathbf{i}}_t = (0, \mp\sin\varphi, \cos\varphi)$, signs being consistent with the corresponding local unit normal $\hat{\mathbf{n}}$ shown in Fig. 2.

We want the unit direction vectors of the beam following reflection in a plane containing the incident beam and local surface normal $\hat{\mathbf{n}}$. In vector algebra, the direction vector for a reflected ray is given by the equation

$$\mathbf{r} = \hat{\mathbf{i}} - 2(\hat{\mathbf{i}}.\hat{\mathbf{n}})\hat{\mathbf{n}}. \tag{2}$$

Ray angles are usually small in the proposed system, allowing the approximation $\cos\theta \approx 1$.

In applying Eq. (2) we need the vectors for the surface normals. Defining a distance d from the cone surface to the original incident beam focus, we can calculate the beam radius $a = d\sin\varphi$ at the surface of the cone. Then from the relationship $\sin\theta = a/r$, valid for small values of θ, we have $\sin\theta = d\sin\varphi/r$, which gives the local normal to the mirrored surface for the intersection positions of the chief ray and for each marginal ray in the incident beam. Knowing $\hat{\mathbf{i}}$ and $\hat{\mathbf{n}}$ for each ray, we can find the direction vectors following reflection at the cone surface. The calculation of the beam radius at the cone surface, $a = d\sin\varphi$, becomes less accurate when the NA is very small and the Rayleigh range extremely large. In the limiting case of a collimated incident beam, a is the (constant) collimated beam radius.

Most ray-trace modelling for the cone mirror was performed using Zemax. However, some simple initial calculations are useful in illustrating the general behaviour of the system. We assume a chief ray (1,0,0) parallel to the system *z*-axis. For marginal rays parallel to the local cone tangent, we then obtain the approximate equation

$$\mathbf{r}_t = \left(1, \pm\left(\left(\frac{d}{r}\right) - 1\right)\sin\varphi, 0\right). \tag{3}$$

For $d < 0$, corresponding to a divergent incident beam, the reflected beam parallel to the cone tangent is also divergent. For a convergent incident beam, with $0 < d < r$, the reflected beam is initially convergent, the reflected NA reducing with d towards a condition of collimation close to $d = r$, thereafter becoming increasingly divergent.

For marginal rays parallel to the cone axis, we obtain

$$\mathbf{r}_a = (\cos\varphi, 0, \mp\sin\varphi) \tag{4}$$

and the NA of the beam is always unchanged on reflection. Thus astigmatism is introduced into the reflected beam, with different focus positions in planes parallel to the tangent and axis

Optics EXPRESS

of the cone respectively. The effect in practice is to limit the useful working distance for sensing applications to values of the order of the cone radius at the reflection point.

For cone dimensions large relative to the beam diameter, surface curvature can be ignored, but as the base radius drops below one order of magnitude greater than a typical beam diameter (around 1-5 mm), the effects on the NA of the reflected beam start to become significant over millimetres rather than centimetres.

3. Custom optical element

In sensing applications, it is desirable to achieve a good beam focus on the internal duct surface. Therefore, a custom optical element was designed, to be used in tandem with the conical mirror with the aim of reducing beam astigmatism following reflection.

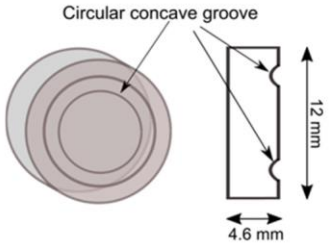

Fig. 3. Schematic 3D representation of, and diametric profile through, the custom cylindrical lens element. Not drawn to scale.

The additional element, shown in Fig. 3, comprises a poly(methyl methacrylate) (PMMA) disc with a diameter slightly larger than the base of the cone mirror. A shallow circular groove 2 mm wide and centred on a ring of 4 mm radius, with a design value of 8 mm for the groove radius of curvature, was machined into the surface of the disc using high-precision diamond-turning [23]. This procedure creates, in effect, a continuous concave cylindrical lens running around the disc, with zero optical power parallel to the local tangent and negative optical power parallel to the local radius. The custom lens has no effect on beam NA in any plane containing a tangent of the element, but the beam experiences reduced NA on reflection at the conical mirror. In planes containing a radius of the custom lens element the opposite is true; there is a reduction of beam NA after the lens element, but no change at the conical mirror. Thus, using the custom lens to produce a judicial introduction of astigmatism into the incident beam, we envisage an improved overall focus at an increased distance from the cone. The groove radius of curvature of 8 mm, corresponding to a focal length of about 16 mm, was selected empirically from modelling (described below) to result in optimum performance at a working distance of about 20 mm from the cone axis, with the input beam set 4 mm off-axis. This allowed experimentation over a good range of input NAs and working distances.

The groove radius of curvature was obtained by treating the custom-made element as a thin lens. This is not strictly correct, as the element has appreciable optical thickness, but provides an adequate estimate for the appropriate radius of curvature. The refractive index n of PMMA at 1330 nm is 1.48, and the focal length of a thin lens is given by the equation

$$\frac{1}{f} = (n-1)\left(\frac{1}{R_1} - \frac{1}{R_2}\right), \tag{5}$$

where R_1 and R_2 are the radii of curvature of the front and back surfaces of the lens respectively. Hence, for a plano-concave lens, the focal length is usually about twice the radius of curvature of the concave surface. For PMMA we have $f = R_1/0.48$. A design radius of curvature of 8.0 mm was selected, corresponding to a focal length of 16.7 mm.

The custom optical element was manufactured at Cranfield. Fabrication was carried out by the Cranfield Precision Engineering Centre, using their high-precision diamond turning

Optics EXPRESS

facility. The original substrate was a 4.6 mm-thick, 12 mm diameter moulded disc of PMMA. The centre depth of the 2mm-wide circular groove, measured from the flat surface, was about 60 μm. The final best-fit radius of curvature was 8.26 mm and the deviation from this value, measured using a Talysurf with a resolution of about 1 nm, was no more than 0.05 μm over the central 90% of the profile. The rms surface roughness was about 0.01 μm. The focal length of the resulting lens, measured parallel to a cone radius, was estimated as 17.2 mm.

4. Zemax beam-waist modelling

The ray-tracing model was coded in Zemax. There is no lower limit to beam diameters in Zemax ray-tracing; foci can become unphysically small and, in lower-NA systems, readily fall below the minimum waist size predicted by Gaussian beam propagation theory. Once beam diameters drop to some tens of microns, the effects of diffraction can no longer be ignored and results from ray-tracing models will be incorrect. Manual calculation was therefore used in addition when necessary, to estimate Gaussian waist radii at focus in the two principal axes of the system following reflection from the cone.

4.1. Cone mirror alone

Initially, the behaviour of the 5 mm radius, 45° conical mirror used alone was examined, for an input beam travelling parallel to the cone axis and impinging on the mirrored surface at a given radius *r* from the axis. The behaviour of reflected beams was examined as the input numerical aperture (NA) was altered. Here, the NA is specified at the width where power is $1/e^2$ of the on-axis power, for consistency with a beam waist radius $w_0 = \lambda / (\pi(NA))$ similarly defined under Gaussian beam propagation calculations.

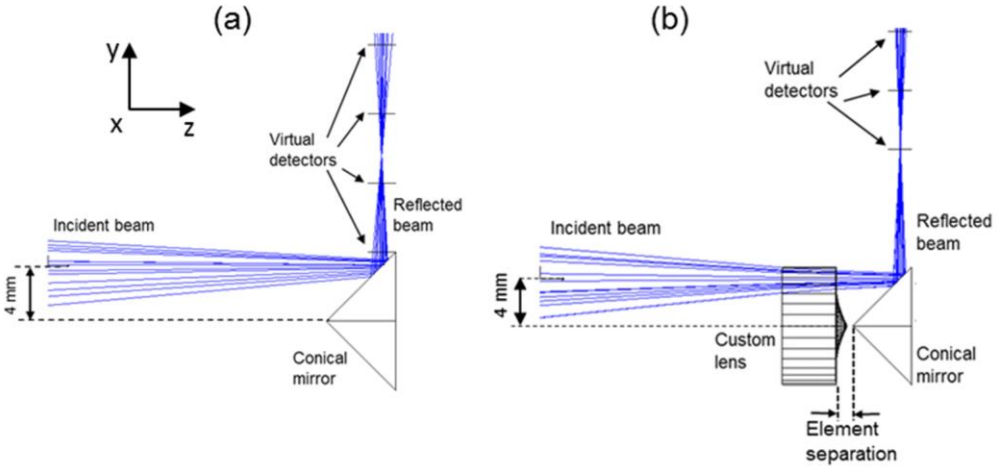

Fig. 4. System geometry used in Zemax modelling to investigate beam focus for (a) conical mirror used alone, also showing the co-ordinate system used throughout, (b) custom lens and conical mirror in combination, with element separation distance defined. Beam centre in each case is 4mm from the cone axis, as shown.

The layout used for modelling beams reflected from the conical mirror alone can be seen in Fig. 4(a). A Gaussian source was used to provide a good approximation to the output from a single-mode fibre. Incident NA was adjusted by altering the distance from the source to the beam focus. Beam profiles can be monitored on 'virtual detectors', placed normal to the beam path at selected *z*-positions. Working distances (defined as radial distance from cone axis to test surface) from a few millimetres to a few tens of millimetres are considered.

Beam profiles obtained depend upon the *z*-position of the cone relative to the original incident beam focus. This offset must be adjusted slightly to achieve best focus for each

Optics EXPRESS

working distance. As expected, the NA change in the tangential plane results in strong asymmetry in beam profiles following reflection. The position of optimum compromise resolution is defined as that providing the lowest waist radius obtainable simultaneously in both astigmatic planes. This beam radius is considerably larger than the best focus in either individual plane considered separately.

Modelled best-resolution beam profiles are shown in Fig. 5(a) for a working distance of 15 mm and several NA values, and a graph detailing the modelled best-resolution focus for a range of working distances and NA values is shown in Fig. 5(b). Each line on this plot corresponding to a particular NA value is a linear fit to four individual data points (also shown on the graph). Noise in the modelled beam profiles can be reduced by increasing the number of rays traced, at the expense of longer computation times. The astigmatism introduced by the cone is sufficiently large that, even for moderate NA values, a reasonable focus can be obtained only within a few millimetres from the cone surface.

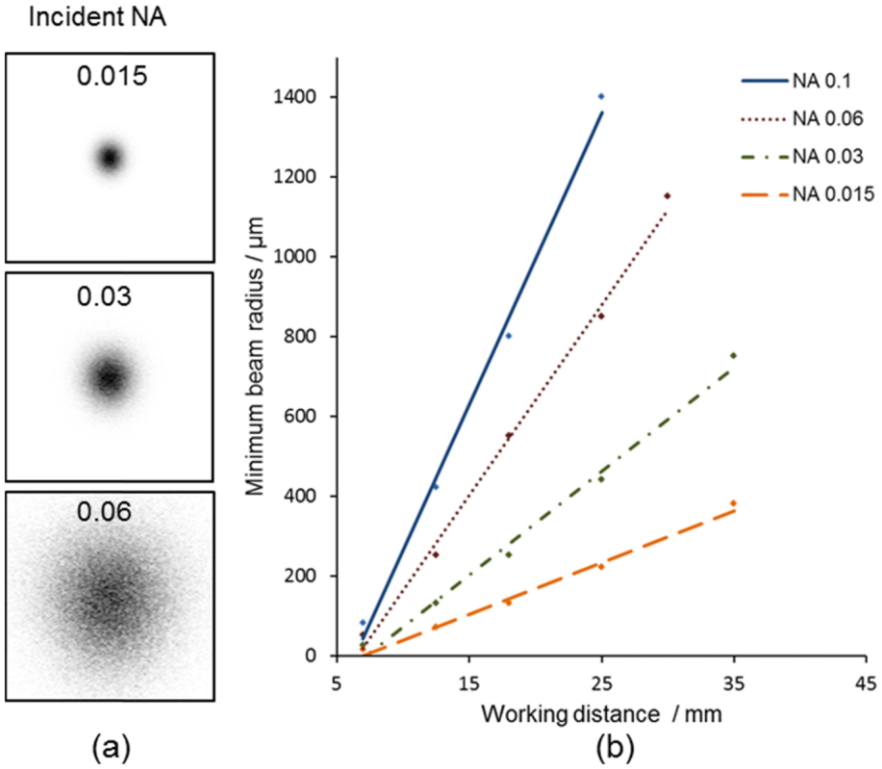

Fig. 5. (a) Best-resolution beam profiles, on a 1 mm square 'virtual detector', from the Zemax model (conical mirror alone), for a working distance of 15 mm, at three different NA values. (b) Beam waist radius at position of optimum compromise resolution, for conical mirror used alone. Symbols represent individual Zemax modelling values, with straight line fits to each data set, for four NA values from 0.015 to 0.1.

In conclusion, for the cone used alone, resolution can be improved only by seeking the best compromise position between the two individual astigmatic foci. Compromise beam waist values are typically well predicted by Zemax. The optimum compromise waist radius increases with NA, as would be expected, since the separation of the two foci is independent of input NA for a given cone radius. It is evident from Fig. 5(b) that, at distances from the cone axis larger than about 10 mm, the compromise focus rapidly expands to hundreds of micrometres in diameter, even at moderate NA values, leading to a severe loss of power density and spatial resolution that prevents the acquisition of low-coherence signals.

Optics EXPRESS

4.2. Conical mirror and custom lens combination

Zemax modelling was repeated with the custom lens incorporated into the system, for the same range of NA values and working distances. The custom lens should mitigate beam astigmatism, reducing beam spot dimensions at the best compromise focus.

Figure 4(b) shows the new arrangement, with the circular groove at a radius of 4 mm from the centre of the additional element. The modelled groove curvature profile extends across the entire custom lens surface, hence a sharp point at the centre of the rear surface, not present on the physical element. To minimise aberrations, the grooved surface of the lens was positioned facing away from the incident beam [24]. The custom element causes an NA reduction in the plane parallel to the probe axis, but no NA change in the perpendicular plane. The working distance depends on the positioning of the cone/custom lens combination relative to the original beam focus. Additional control over the relative positions of the two astigmatic beam foci is gained by varying the separation between the custom lens and conical mirror.

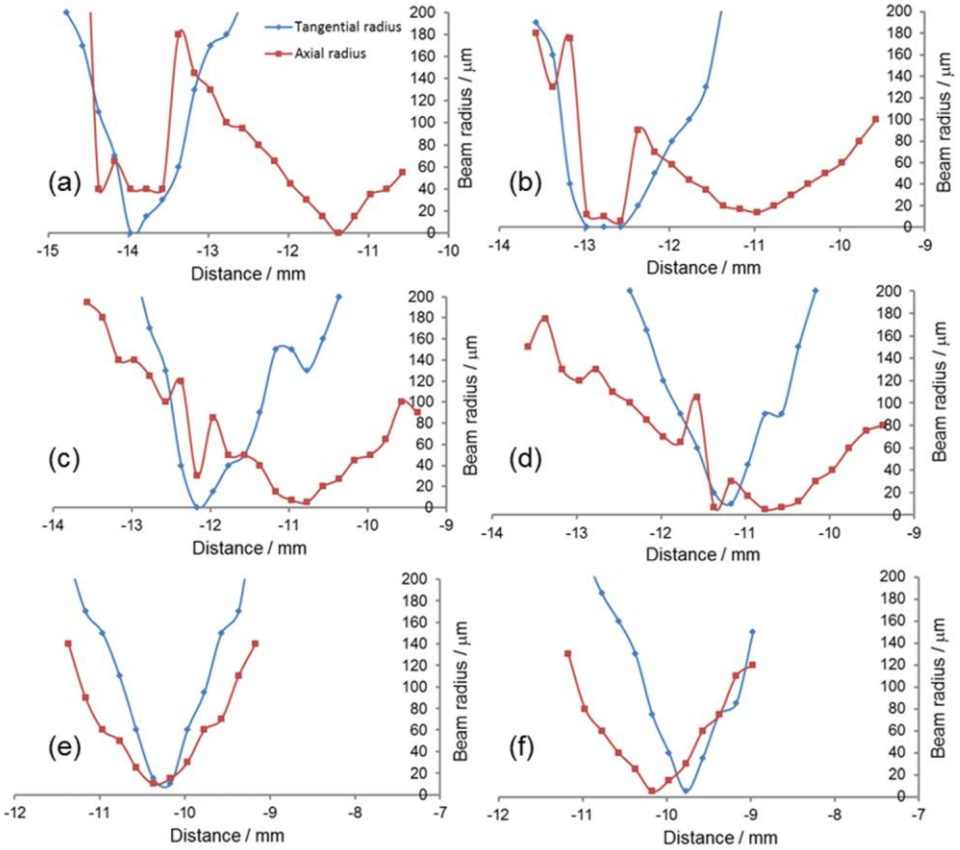

Fig. 6. Plots from Zemax modelling, showing the evolution of axial and tangential beam waists as the custom lens/cone element combination is tracked parallel to the optical *z*-axis. Abscissae show distance from the original focus to the front surface of the custom lens. Plots assume a working distance of 12.5 mm, input NA of 0.06 and element separations of (a) 4.0 mm, (b) 2.8 mm, (c) 2.1 mm, (d) 1.5 mm, (e) 0.5 mm, (f) 0 mm. Legend in (a) applies to all plots.

The custom lens was incorporated before the conical mirror, with a variable separation between the custom lens and the cone, as shown in Fig. 4(b). A range of working distances was investigated as optical element separation and input NA were varied. For each set of input values, the cone/custom lens combination was tracked in *z* (parallel to the probe axis) to locate the best compromise beam waist at the desired working distance. Slight adjustment of

Optics EXPRESS

the separation distance between the custom lens and the tip of the conical mirror can further reduce the separation between the positions of the two astigmatic foci.

Figures 6(a)-6(f) present the modelled evolution of axial and tangential beam radii around the position of optimum focus, for a working distance of 12.5 mm and an input NA of 0.06. In each graph, abscissa values represent the *z*-position of the custom lens element (front surface), given as the distance from the original beam focus. This distance must be adjusted to optimise focus for a particular custom-lens/cone separation. It can be clearly seen that, as the element separation is reduced from 4 mm towards zero, the two astigmatic foci move closer together and, for an optimum element separation of 0.5 mm, coincide, as seen in Fig. 6(e). In this situation, Zemax predicts an average minimum beam radius of a few μm, with beam-waist dimensions remaining below 100 μm for axial positioning errors up to about ± 1 mm.

The optimum separation of the optical element pair varies for different working distances (WDs), but in all cases an excellent focus is predicted when the element separation is correctly set. Acquisition of plots analogous to those of Fig. 6 resulted in values for the optimum element separation of: –0.15 mm at a WD of 7mm, 1.8 mm at a WD of 18 mm and 3.1 mm at a WD of 25 mm. We note that the appropriate element separation for the 7 mm working distance is negative, implying that the tip of the conical mirror must be positioned *before* the rear surface of the custom lens. Hence this situation can be realised in practice only by cutting away the tip of the conical lens.

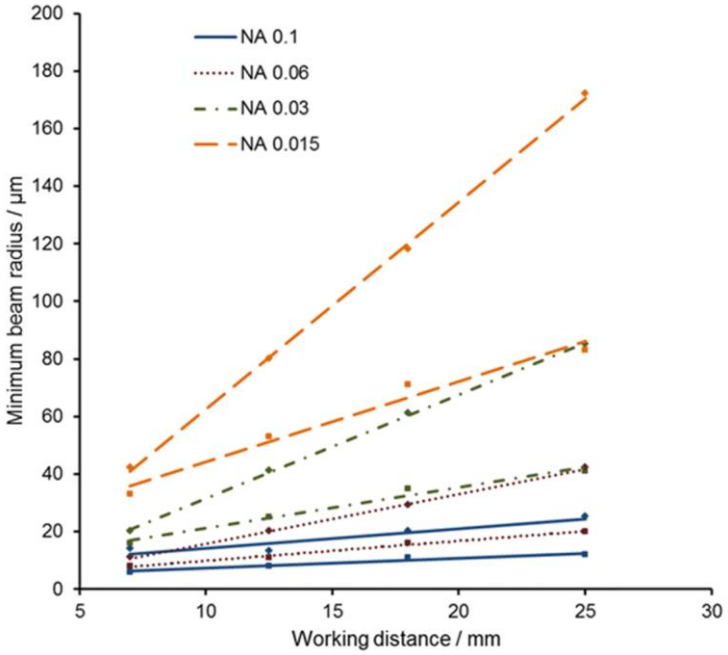

Fig. 7. Axial (squares) and tangential (diamonds) beam waist radii, at the position of optimum compromise resolution, from modelled profiles for conical mirror and custom lens element used together. Straight line fits to each data set are also shown, for NA values of 0.015 to 0.1.

The model predicts that the dual-element system can bring the two foci into close coincidence over a wide range of working distances. Axial and tangential beam radii, for the smallest beam spot obtainable at different WDs, are shown in Fig. 7. For the modified dual-element system, beam radii, and hence spatial resolution, are better predicted in practice by substituting the appropriate Gaussian diffraction limited beam waist radii in both principal planes, following reflection from the cone. These are the values displayed in Fig. 7. As before, there is some uncertainty in the modelled beam waists, largely now because of small errors in estimating post-reflection beam NA values.

Optics EXPRESS

For an optimised system, an improvement of a factor of two in resolution, averaged over axial and tangential values, is predicted even at the lowest input NA of 0.015. Modelling indicates that inclusion of the custom lens can reduce optimum beam-spot dimensions by up to one order of magnitude at input NA values approaching 0.04, and offers an even greater advantage at NA values approaching 0.1, compared with best-focus radii obtained from the conical mirror alone. The greatest advantage at any particular working distance is gained by choosing a lens element of the correct power to bring the two beam foci as close together as possible. A lesser advantage is obtained even from an imperfectly specified lens.

In conclusion, the predicted beam-waist improvement should greatly extend accessible working distances for low-coherence measurements, particularly at higher values of input NA. Modelling results are discussed further below in the context of comparison with experiment.

5. Passive probe head construction

Our prototype low-coherence tube-profiling system is a ‘passive probe’, in which the conical mirror is addressed by an array of single-mode fibres arranged on an arc of a circle concentric with the cone.

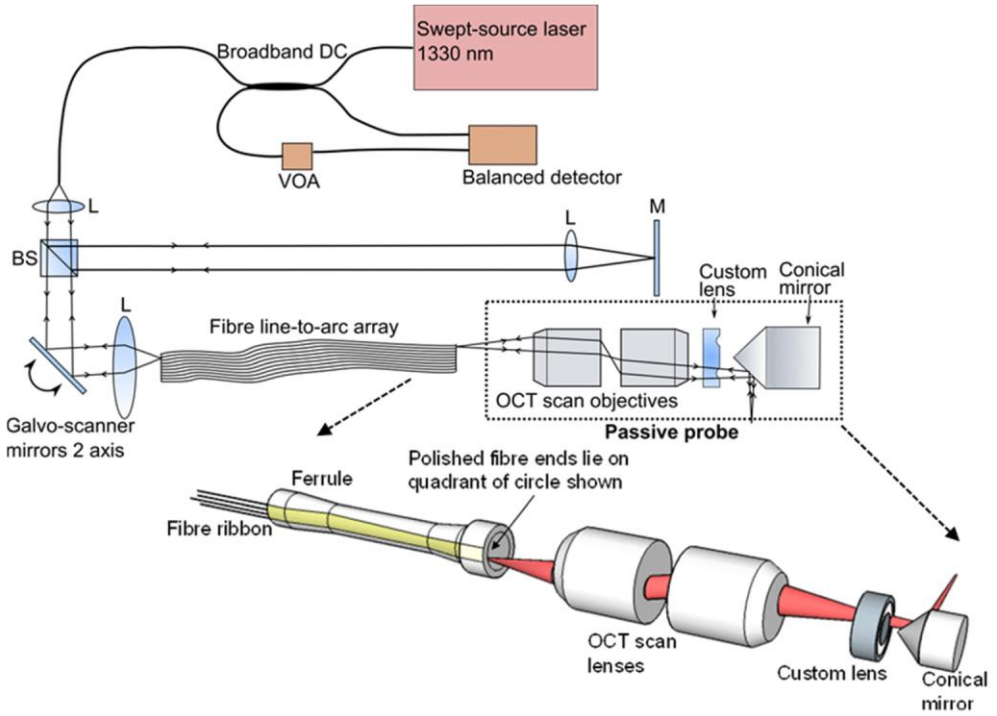

Fig. 8. Schematic of the optical arrangement, showing the broadband fibre coupler used for beam delivery and the bulk-optic low-coherence Michelson interferometer incorporating passive probe head. DC: directional coupler, VOA: Variable optical attenuator, BS: 80/20 beam-splitter, L: lens, M: mirror. Expanded 3D schematic below depicts optical probe-head components with example ray paths for a single fibre.

Light is delivered to the probe head via a single-mode fibre ribbon array about 0.5 m in length, fabricated in-house. At the output to the probe head, the fibres of the array lie on the circumference of a quarter-circle of 4 mm radius.

The optical low-coherence arrangement is shown schematically in Fig. 8. Light from a Santec HSL-2000 swept-laser source, with a centre wavelength of 1330 nm and a sweep range of 100 nm, is divided by a 50/50 ultra-broadband directional optical-fibre coupler. One output arm delivers light to the low-coherence system, comprising a bulk-optic Michelson

Optics EXPRESS

interferometer. An 80/20 beam-splitter cube further divides the optical power, directing 20% into the reference arm and 80% into the measurement arm. A 2-axis galvo-scanner, in a telecentric focusing arrangement, is used to scan the beam rapidly between individual fibres of the array. The focusing lens used here has a 50 mm diameter, to minimise off-axis aberrations and to prevent vignetting for fibres towards the ends of the linear array.

Light is transmitted by the fibres of the array to the compact probe head, comprising two Thorlabs LSM03 telecentric scan lenses, the custom lens and conical mirror, and allowing different positions on the internal wall of the quasi-cylindrical sample to be addressed at will by selection of the appropriate input fibre. The source bandwidth of 100 nm implies a coherence length of 7.8 μm, defining the depth resolution for low-coherence measurements. Scattered power from the sample wall returns through the optical interferometer and the coupler to a balanced detector. A variable optical attenuator allows removal of the DC background to improve signal-to-noise performance.

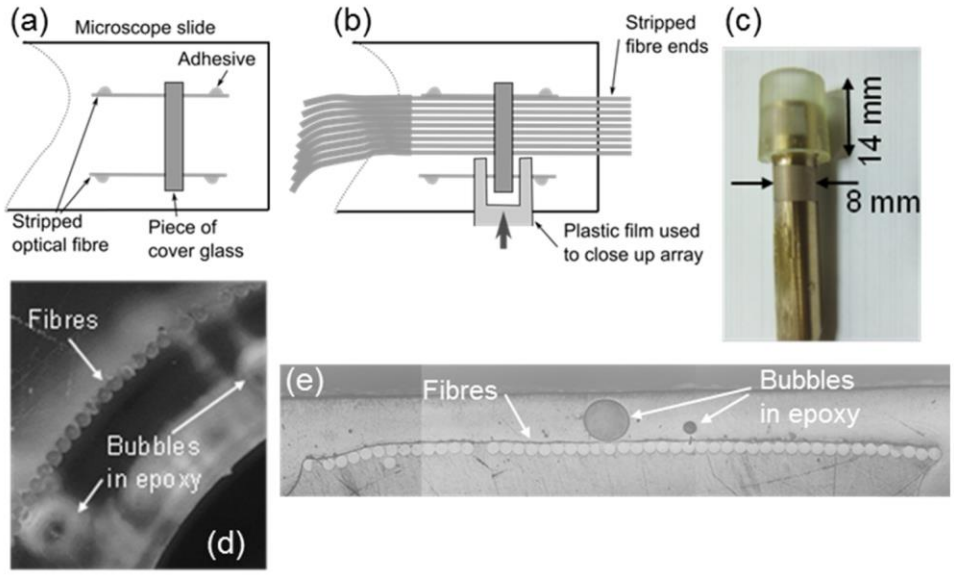

Fig. 9. (a) Construction of 125 μm deep channel for laying up fibre array. (b) Channel loaded with fibres, inserted beneath the cover glass 'roof' and pushed back for equal overlap, showing notched plastc film used to apply pressure to close up gaps. (c) Photographic side view of curved array end on brass mandrel after assembly, potting and polishing. Fibres can be seen on upper surface of mandrel. (d) End-view microscope image showing portion of curved array face. (e) End-view composite of three light-microscope images, showing linear array face.

The fibre ribbon was constructed using 125 μm diameter standard telecommunications single-mode fibre SM1322 P3022-E supplied by Optical Fibres, Deeside (now Corning Optical Fibres), appropriate for the laser centre wavelength of 1330 nm. Fibre was wound in a single layer onto a cylindrical spool and cut perpendicular to the fibre axis to create many strands of equal length. A few centimetres of acrylate coating were removed, using Nitromors paint stripper, from either end of the cut lengths.

To lay up each end of the array, a custom jig was constructed on a glass microscope slide. Two lengths of stripped fibre, separated by about 1 cm, were attached to the slide using cyanoacrylate 'Superglue' as seen in Fig. 9(a). Figure 9(b) shows a sliver of microscope cover slip glass was glued down across the top to create a channel with a well-specified depth of 125 μm, into which stripped fibre ends were inserted to form a single-layered ribbon. Fibre tips were pushed back to overlap the base by a fixed distance. Lateral pressure was applied to close gaps, until fibres lay adjacent and in contact, in a single layer, and 'Kapton' polyimide adhesive tape was applied from above to hold the fibres in place.

Optics EXPRESS

The stripped ends were potted by applying two-part UV-cure epoxy resin over and around the fibres and the end of the glass slide, then a hand-polishing kit was used to expose the array of fibre ends and polish to an optical finish.

The fibre arc at the output end of the array was constructed similarly, with additional strips of Kapton applied to the assembled flat array at the stage shown in Fig. 9(b). This end was then curved around a 4 mm radius cylindrical brass mandrel, the fibres subsequently being potted and polished back, as before. At this end, a high-hardness two-part heat-cured resin (Opti-tec OPT5007-4G) was used for potting. Photographs of the curved array end after finishing are shown in Figs. 9(c) and 9(d), and a view of the linear end in Fig. 9(e). The linear end is not perfect; one fibre is completely out of position, a couple of others are imperfectly polished and the array does not lie perfectly flat to the slide. However, galvo-scanner voltages can be individually adjusted to ensure good coupling to each fibre. The dark circles visible in the layers around the fibres are air bubbles in the epoxy used for potting. The completed ribbon comprised an array of about 50 fibres. At the output end, the fibres lay on an arc of 4 mm radius forming approximately one quarter of a full circle.

A commercial opto-mechanical system offers a good compromise between compactness, rigidity and adjustability. The completed mandrel was supported by a Thorlabs 30 mm tube system, using two drilled plates as shown in Fig. 10. Three-point support at the second plate allowed the origin of the array to be adjusted relative to the probe axis, and z-adjustment of the mandrel relative to the first lens was also possible.

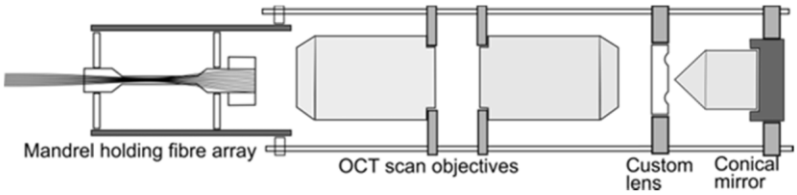

Fig. 10. Detailed view of passive probe head, showing the 30 mm combined tube and cage system used to support the optical components.

The output end of the fibre array was imaged, at unit magnification, through a pair of telecentric OCT scan objectives. The radii of both the fibre arc array and the mid-point of the custom lens groove are 4 mm, hence, with the system properly aligned, the chief ray for beams exiting the second scan objective is centred on the mid-point of the custom lens groove and strikes the cone mirror at a radius of 4 mm from the cone axis. The cage system permits full radial output access for measurement beam. In the present quadrant system, it was possible to rotate the mandrel such that no output beam was impeded by the presence of a rail.

A Vernier screw arrangement clamped to the rails allowed the conical mirror and custom lens to be moved axially, together or separately, with respect to the other optical elements, enabling a range of working distances to be accessed.

5.1. Fibre-to-fibre mapping

Fibres occupied different positions within the array at either end of the ribbon. Initially, the voltage pair required to drive the horizontal and vertical galvo-scanner mirrors to couple light into each fibre in turn was identified, and the array of voltage pairs stored in the control programme, permitting scanning of all array fibres within a few milliseconds. Corresponding indices at the output end were found by coupling 830 nm broadband SLD light sequentially into each array fibre, and imaging the output face onto a visible-spectrum USB microscope camera via the integral lens. The centroid of the beam spot produced from each output fibre was obtained to an accuracy of about ± 0.5 pixel, allowing a map, shown in Fig. 11(a), to be constructed of fibre positions at this end of the ribbon. Also, pixel co-ordinates for the centre axis and a diameter of the mandrel were obtained from a white light camera image, and used

Optics EXPRESS

for distance scaling of the 8 mm diameter mandrel end-face. This information was used to calculate, for each y-value, the corresponding x-value for a fitted circle 4.06 mm from the mandrel centre position, allowing for the 125 μm fibre diameter.

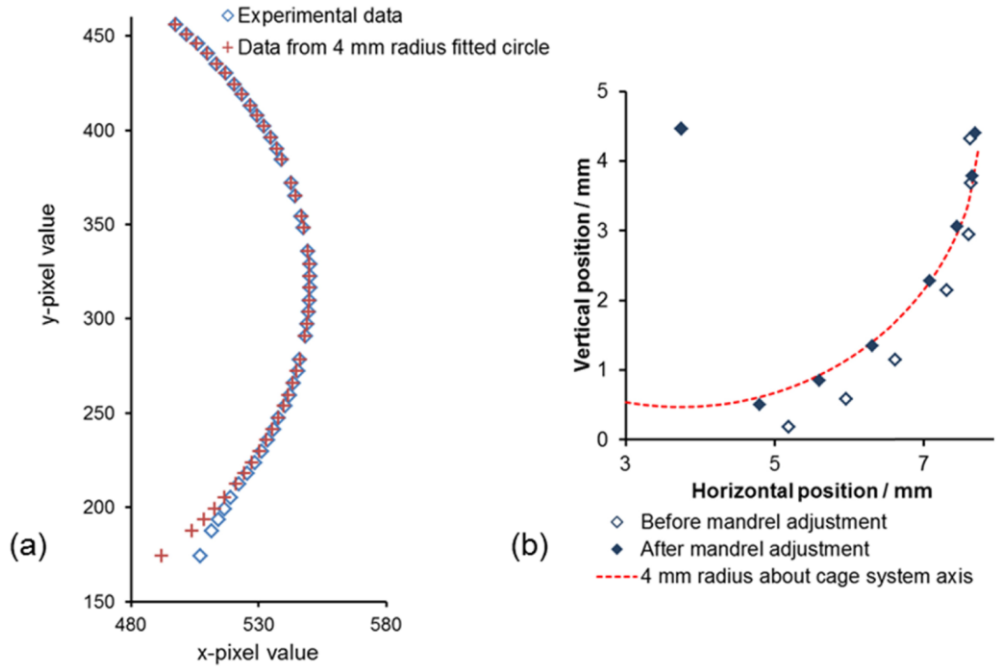

Fig. 11. (a) Centroid positions of fibres at output end of fibre array, from camera image of array output face. (b) Positions of selected array fibres with respect to cage-system axis, before (hollow markers) and after (solid markers) mandrel adjustment. The red dashed line shows a circle of radius 4mm, concentric with the mounting-system axis.

Agreement between experimental and fitted data, shown in Fig. 11(a), is generally excellent, demonstrating that fibres lie regularly spaced in close lateral contact, and adjacent also to the surface of the mandrel. The last four or five fibres have lifted from the surface by a few tens of micrometres, and a few other fibres are missing or damaged such that insufficient optical signal is obtained, but 44 usable fibres exist within the array.

5.2. System alignment

When mounting the arc array in the optomechanical system, concentricity of array and cage system axes is important to ensure good performance. The cage system axis was first located. An output end of the fibre coupler was mounted within the 30 mm tube section of Fig. 10, at the correct working distance for the first scan lens, using a threaded mounting plate. At this stage the custom lens and conical mirror were absent from the system. A 40 μm spatial-filtering pinhole was positioned at the beam focus in image space, following the second scan lens. The pinhole was adjustable in 3 axes to allow maximisation of power transmission. Six repeats were performed with the fibre mounting plate rotated to different angular positions, resulting in six sets of pinhole x-y coordinates. Centre-axis coordinates were calculated as the mean values of x and y, the resulting standard deviation being about ± 50 μm.

Next, the single central delivery fibre was removed and the arc array substituted in the mounting system, at the correct distance from the scan lens to ensure unit magnification imaging. Light was coupled into a selection of the array fibres, and beam foci x-y co-ordinates in image space located as above. Anomalous fibres at the left-hand end of the arc were avoided. The results are shown in Fig. 11(b). Initially the array was not correctly positioned

Optics EXPRESS

(hollow markers in the figure). However, following mandrel adjustment using the three-point mounting screws in the second plate, good concentricity was obtained (solid markers), with a worst-case deviation of no more than ± 100 μm from the correct position.

The focal length of the input lens was larger than that of the source collimator, reducing beam NA below the optimum value for the array fibres with some resultant loss of coupled power. This could be improved by grouping input-end fibres within a smaller outer radius, perhaps in several shorter rows, allowing for a smaller, lower focal length input lens.

5.3. Depth correction

The reference arm length is common to all measurements, but length variations up to a few hundred micrometres in the lengths of individual sample-arm array fibres are unavoidable. Variations are therefore also seen in measured depth for a flat sample, using different fibres. This can be investigated by inserting a flat mirror at the beam-focus position in image space, and locating the mirror peaks in the low-coherence signals observed at the balanced detector.

The laser coherence length, and hence system resolution in the original data, is 7.8 μm. At the original sampling density of 1024 points per scan, a single pixel in the low-coherence data following Fourier transform corresponds to a depth change of 7 μm, hence the signal point-spread function is not well sampled and zero-padding by a factor of 4 was used routinely to improve location of the peaks to ± 1.8 μm [25].

Individual measured depths from an optically-flat mirror deviated from a straight-line fit by up to 300 μm. The standard deviation of the errors was 85 μm. To correct for observed differences, length errors derived from three similar sets of data were averaged, and the average error for each fibre subtracted from all subsequent measurements. The standard deviation was now only 4.1 μm, demonstrating that errors due to fibre length variation have been removed. An increased zero-padding factor could further reduce this scatter if required.

Finally, the conical mirror and custom lens were incorporated, precise mechanical measurement ensuring concentricity of the centre axes with those of the mounting plates.

6. Experimental measurements from completed probe system

6.1. Beam-waist measurements without and with custom lens

Measurements were carried out with the conical mirror alone, then with conical mirror and custom lens combined, to find the best-focus spatial resolution of the probe system at different radial working distances from the cone axis. An NIR InGaAs camera (Vosskühler NI-300) was used for beam profiling. Significant magnification was required to overcome the resolution limitations of the 30 μm x 30 μm pixels, so a well-corrected relay lens was used to throw an image of the beam focus, at high magnification, onto the camera sensor, mounted to the side of the probe at a distance of 300 mm. With the camera at this distance from the outer edge of the cage mount, magnification was between 16.5 and 17.7 for all measurements, varying a little as the relay lens was shifted to access different working distances. For larger beam spots/working distances, the camera distance from the outer edge of the cage mount was approximately halved, magnification values now ranging from 6.7 to 8.8.

Light was delivered through a single fibre of the ribbon array such that the beam reflected from the conical mirror ran parallel to the surface of the optical bench. This simplified the relay lens set up, allowing components to be mounted directly on the optical bench.

For system measurements with the conical mirror alone, the custom lens was removed, the relay lens was set to image the beam profile at a selected working distance, and the longitudinal distance of the cone relative to the original beam focus, was adjusted to produce the smallest possible beam spot on the camera. Under these conditions, beam profiles obtained were very close to circular as predicted by modelling. The measurement was repeated for a range of working distances up to 25 mm from the cone axis. It was difficult to measure beam profiles for longer working distances because the best-focus beam radius

Optics EXPRESS

rapidly became very large and the intensity profile within the beam spot rather variable, possibly because of imperfections in the surface quality of the conical mirror.

The evolution of best-focus beam waist radii from using the conical mirror alone is shown in Fig. 12 (blue circles). A linear fit to the data is consistent with the Zemax modelling seen in Fig. 5, with values suggesting an NA of about 0.025.

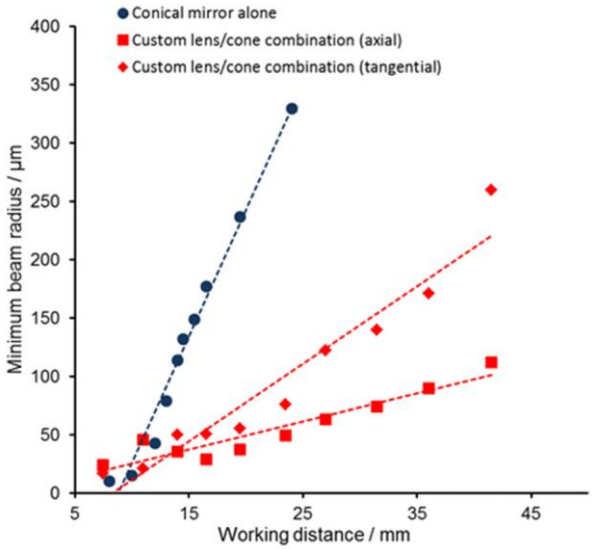

Fig. 12. Experimental beam-waist radii at best focus for the low-coherence probe. Blue circles are values for the conical mirror used alone. Red markers are axial (squares) and tangential (diamonds) values for the conical mirror and custom lens element used together.

The custom lens was reintroduced into the system and best-focus beam waist measurements were repeated for the custom lens/conical mirror combination. As before, the relay lens was adjusted longitudinally for different working distances. The custom lens/conical mirror spacing was adjusted, then the two elements tracked together to seek the new best focus. Iterative spacing adjustment, followed by tracking of the element pair, for each working distance, determined the element spacing for which axial and tangential beam waist values were simultaneously minimised.

The evolution of best-focus beam waist radius from experiments with the combined element pair is also shown in Fig. 12 (red squares: axial beam waist radii, red diamonds: tangential beam waist radii). It is immediately clear that the beam-waist dimensions are significantly reduced by use of the custom lens, as predicted by modelling, and this allowed us to measure beam-waists, with good optical power density, out to radial working distances of 45 mm and beyond. Linear fits to the axial and tangential beam-waist radii data result in plots that look very similar in form to those of Fig. 7. There are small discrepancies between experimental points and the linear fit, particularly at lower working beam-waist values, the most likely cause being small errors in the experimental setup, either in the form of lateral offsets or angular offsets from the main system axis. As for the conical mirror alone, experimental values, when compared with the data in Fig. 7, are consistent with a probe-system NA between 0.025 and 0.03.

The NA of the optical fibre used to deliver the beams to the measurement region is about 0.1, and the scan lenses are quoted as having an NA of 0.056. NA is further reduced by the combined arrangement used in this system. As stated above, Fig. 12 indicates that our experimental system appears to operate with an NA of between 0.025 and 0.03. Despite power losses caused by NA mismatches, and focused beam-waist values of several tens of micrometres, low-coherence signals were readily obtained from metallic and polymer surfaces

Optics EXPRESS

at working distances exceeding 45 mm from the cone axis, whereas with the conical mirror alone it is difficult to obtain a signal of sufficient magnitude for working distances exceeding 15 mm. For all distances above about 10 mm from the cone axis, the custom lens offers a large benefit in improving spatial resolution and signal magnitude. Very close to the cone surface, no apparent benefit was observed from this particular custom lens, although a similar element with a different specification would be expected to improve resolution even here.

6.2. Low-coherence profiling

The performance of the probe was now assessed for acquisition of low-coherence profiles from a series of quasi-cylindrical test pieces. Test samples, shown in Figs. 13(a)-13(e), produced on an Ultimaker 3D printer, were designed with locating notches to slot over the rails of the cage system around the conical mirror. The tubular surfaces, coloured red in Figs. 13(a)-13(d), of the four test pieces had radii of curvature of 8 mm, 12.5 mm, 18 mm and 25 mm respectively. The in-plane spatial resolution of the 3D printer is quoted as 40 μm. In the open-source software used to draw models for our 3D printer, and during the 3D print process, arcs are approximated by concatenating many linear segments, the number of segments in a whole circle being user-defined. For test-piece radii of 8 mm, 12.5 mm and 18 mm, we used 30 linear segments per 360°, while for the 25 mm radius test-piece we used 44 segments per 360°. Reflectivity was increased by applying 30-μm thick, self-adhesive reflective foil, sufficiently thin and conformable to follow variations in surface flatness.

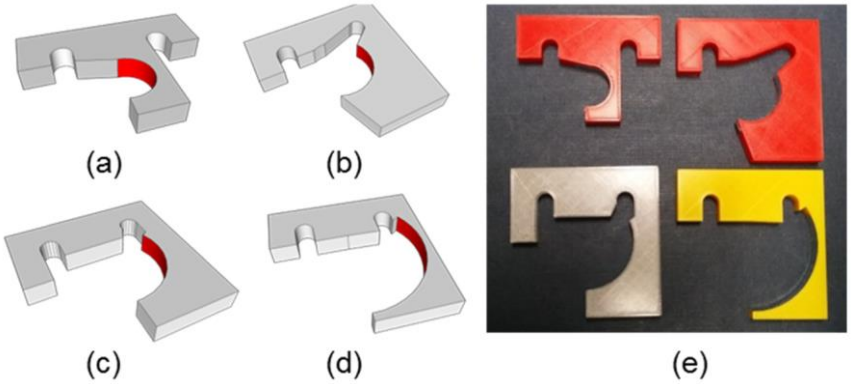

Fig. 13. Schematic diagrams of tube-section samples used for testing the low-coherence profiling system. Radius of curvature of the test surface (shown in red) is (a) 8 mm, (b) 12.5 mm, (c) 18 mm and (d) 25 mm. (e) Photograph of the four 3D-printed samples.

For each test piece, the spacing between the custom lens and conical mirror was adjusted, with reference to Fig. 6, to allow placing of the best compromise focus at a working distance appropriate to the average test-cylinder radius and the optical beam was scanned to each array fibre in turn to address positions around the circumference of the tube profile.

6.3. Results and discussion: probe measurements

Results from test-piece profiling are shown in Figs. 14(a)-14(d). Low-coherence depth measurement yields only relative distance; it does not allow determination of absolute cylinder radius. However, this is unimportant when variations in radius, or surface defects, are the features of interest. The raw profiles here represent depth measured relative to an arbitrary distance defined by the optical path length in the reference arm.

Optics EXPRESS

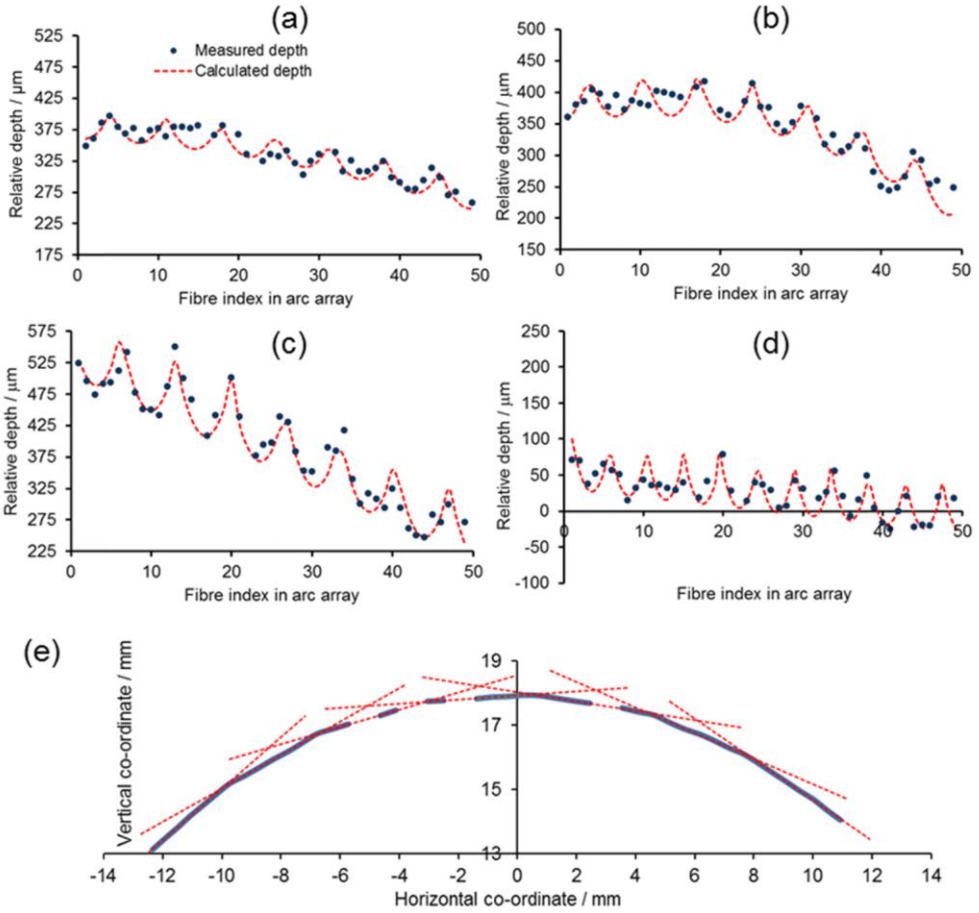

Fig. 14. Low-coherence surface depth profiles (blue points) from 3D-printed tube-section test samples having radii of curvature: (a) 8 mm, (b) 12.5 mm, (c) 18 mm and (d) 25 mm. Red dotted lines show the expected periodicity from theoretical calculation. (e)Plot of the measured depth information from (c) superimposed on a circle of radius 18 mm (blue solid line). The individual line segments from which the arc is constructed can be identified, and are highlighted by linear fits (red dotted lines) to the appropriate data subsets.

For all four test pieces, periodic variation in measured depth is seen in the raw data profiles as the beam is stepped from fibre to fibre, sweeping through a quarter of a circle. This periodicity is explained by the linear segmentation described above. Depth measured from the tube axis is greater towards the vertices of each linear segment and smaller towards the segment centre. A slower, non-periodic variation in measured depth is also seen in the graphs, arising from x and y offsets between the probe axis and the axis of the test piece. This variation can be approximately linear, or have significant curvature, depending on the magnitude and relative sign of the two offsets.

The periodic depth variation expected from the segmented geometry has also been calculated, and superimposed on the slower variation calculated from a polynomial fit to the original data points. It can be clearly seen that the overall shape, magnitude and frequency of the low-coherence depth measurements are a good fit to the values calculated from the known segmentation. The three lower-radius tube-sections are all constructed from seven linear segments; we find, as expected, that the measured linear segmentation is more clearly apparent, and the magnitude of depth oscillation greater, as circle radius increases. For the largest, 25 mm radius tube-section, the number of segments used has been increased to about

Optics EXPRESS

eleven, therefore the frequency of depth oscillation also increases, although its magnitude is somewhat reduced. Departures from the theoretical curve occur in places. The standard deviation of these departures, averaged over all four plots, is about 17 μm, considerably larger than the low-coherence depth resolution of around ± 4.5 μm obtained previously from a flat mirror surface. However, the variation is reasonably consistent with the 40 μm resolution quoted for the 3D printer. We conclude that the observed depth variation is dominated by real surface quality errors resulting from the 3D printing process, not by inaccuracy of the low-coherence measurement.

Figures 14(a)-14(d) display deviation from mean tube radius. A more intuitive representation of the same data can be obtained by superimposing these depth variations on circles of radii corresponding to each of the test-pieces. An exemplar polar plot resulting from this procedure is shown in Fig. 14(e) for the 18 mm radius test piece, for which segmentation of the 3D-printed tube should be most clearly apparent, and is indeed discernible in Fig. 14(e). Superimposed linear fits (in red) have been overlaid on individual segments to aid identification, and it can be seen that there are just over 7 segments in the full quadrant, consistent with the segment angle of 12° used by the drawing package.

Good probe centration within the duct minimises differences in measured depth values, which must fall within the limited range of the low-coherence technique. This is typically only a few millimetres, though it can be extended by increasing sampling density. Additionally better signals are obtained for beams near-normal to the surfaces, particularly if surfaces are optically smooth. Lateral resolution, once optimised for a given working distance, deteriorates quite rapidly within a few millimetres to either side of this distance. Hence although perfect concentricity is not necessary, it is desirable for the measurement probe to be mounted close to the centre axis of the duct.

For practical use, an engineered probe in a lighter, cylindrical casing would be a better solution, allowing the device to be held centrally within a sprung cage or balloon catheter, as appropriate.

7. General discussion

For surface profiling, it is not always critical to reduce focused beam-waist radii to the very small values typical for structural low-coherence imaging. Indeed, this is not generally possible at working distances of tens of millimetres. When the system input NA is low, the depth of focus is high, and beam radii remain almost unaltered over long distances. This allows significant leeway in the relative positioning of the two foci for the axial and tangential components of the beam. As a first approximation, the aim should be (from Eq. (3) to set $d \approx r$ and to bring the tangential beam component close to collimation. The position of focus for the axial component is then fixed by the optical power of the custom lens and by adjustment of the distance between the custom lens and conical mirror. For input NA values below around 0.05-0.06, beam radii are relatively weak functions of position. An almost constant, few tens of μm beam radius can be achieved over a working distance range of many millimetres even for a non-optimal custom lens. Input NA values below about 0.015-0.02 are less appropriate because, although the depth of field can be many tens of millimetres, beam-waist radii rise above 100 μm even for moderate working distances.

If 3D information is required, a series of cross-sectional profiles can be obtained by drawing the probe back through the duct at a constant rate as data is acquired, with the longitudinal data density set by the draw-back speed [26]. At a working distance of 25 mm, the average spatial resolution is set by the mean beam waist radius of around 70 μm, but the circumferential data-point spacing is currently 780 μm. For shape profiling, this might be more than sufficient, but for defect detection a greater circumferential data density would be preferred. It is relatively straightforward to double the density using commercially-available 50 μm diameter optical fibre for the fibre arrays. Further increase is more difficult, though custom optical fibres with cladding diameters of 30-40 μm can be obtained. A dual ring of 50

Optics EXPRESS

μm fibres at the probe end, with outer fibres nested between each adjacent pair of the inner ring, would provide a good compromise solution.

Modelling predicts that, in principle, it should be possible to obtain beam-waist radii, even at working distances a factor of 5 greater than the cone radius, approaching those suitable for structural OCT imaging. To achieve this would require an input NA of around 0.07-0.1. In this input NA range, depth of field at the duct wall is reduced to a few hundred μm and it becomes imperative that the focus positions in both axial and tangential axes are brought into close coincidence to ensure good lateral resolution. The custom optical element must now be designed for a specific input NA and working distance. Good results will be strongly dependent upon aberration control and excellent experimental alignment. It is debatable whether this can be adequately achieved in practice. The relative data-point sparsity inherent to a passive probe of this type is also less well suited to OCT imaging applications. Our results suggest, however, that significant benefits are to be gained in improving the potential of such a system for the purposes of duct inspection and profiling, where resolution and data density requirements are generally somewhat more relaxed.

Extending the technology to a full ring of fibres would allow the acquisition of diametrically-opposed measurements which, relative to a standard test cylinder, would enable pipe diameter measurements to be obtained with high accuracy and precision, in addition to the simpler surface profiling capability.

8. Conclusions

A compact, passively-addressed low-coherence probe, with a depth resolution of 7.8 μm, has been constructed for the profiling the internal surfaces of pipes and other quasi-cylindrical ducts. Removal of rotating components from within the probe head avoids the need for electrical wiring and signals within the probe head; an advantage for monitoring pipes that carry flammable or explosive substances. Avoiding rotation also reduces the potential for zero-position errors in high-resolution measurements.

Astigmatism of the beam, introduced by the 5 mm radius conical mirror used to turn the beam through 90°, has been mitigated by the use of a custom cylindrical lens. Our modified probe achieves a reduction in the average beam-focus radius by a factor of about 4, over distances up to 45 mm from the cone axis, compared with use of the conical mirror alone. Greater improvements could be expected in a higher NA system. Both lateral resolution and signal-to-noise ratio are improved, allowing measurements to be made over working distances about four times greater than for the conical mirror used alone, and potentially up to an order of magnitude greater in higher NA systems. The probe has been successfully demonstrated in the laboratory for profiling of test samples from 8 to 25 mm radius.

Funding

Royal Society UK (Paul Instrument Fund PI120020); Engineering and Physical Sciences Research Council UK (EPSRC) (EPN002520/1).

Acknowledgments

We thank Mr Stephen Staines for advice on adhesives and machine-tool tolerances, and manufacture of probe components including the brass mandrel, customised mounting plates and a potting well for the curved array end. The underlying data can be accessed through the Cranfield University data repository at 10.17862/cranfield.rd.4557601

138.250.27.251 {ts '2017-04-18 03:54:34'}

https://dspace.org/

Passively-coupled, low-coherence interferometric duct profiling with an astigmatism-corrected conical mirror

Ford, Helen D.; Tatam, Ralph P.

2017-04-06
Optical Society of America
http://dx.doi.org/10.1364/OE.25.008896
Ford HD, Tatam RP. (2017) Passively-coupled, low-coherence interferometric duct profiling with an astigmatism-corrected conical mirror. Optics Express, Volume 25, Issue 8, 2017 pp. 8896-8915

Downloaded from a DSpace repository. https://dspace.org/